



# Modelling and Ni/Yttria-Stabilized-Zirconia pattern anode experimental validation of a new charge transfer reactions mechanism for hydrogen electrochemical oxidation on solid oxide fuel cell anodes

Weifang Yao, Eric Croiset\*

Department of Chemical Engineering, University of Waterloo, 200 University Avenue West, Waterloo, Ontario N2L 3G1, Canada

## HIGHLIGHTS

- A kinetic model for elementary reactions of  $H_2$  electro-oxidation was developed.
- A new  $H_2$  reaction mechanism was validated using pattern anode experiments.
- Good agreements between simulation and experimental results were obtained.
- Effect of surface diffusion proved to be negligible under investigated conditions.
- Rate limiting steps were elucidated, depending on operating conditions.

## ARTICLE INFO

### Article history:

Received 1 June 2013

Received in revised form

19 September 2013

Accepted 21 September 2013

Available online 30 September 2013

### Keywords:

Solid oxide fuel cell

Ni/YSZ pattern anode

$H_2$  electrochemical oxidation

Kinetic modelling

## ABSTRACT

Good understanding of the  $H_2$  electrochemical reaction mechanism helps optimize SOFC anode design and improve its performance. Controversies still exist regarding  $H_2$  oxidation mechanism despite extensive studies performed. In this work, a new charge transfer reactions mechanism proposed by Shishkin and Ziegler (2010) based on Density Functional Theory (DFT) study was investigated through kinetic modelling and pattern anode experimental validation. The new charge transfer reactions mechanism considers hydrogen oxidation at the interface of Ni and YSZ. It involves a hydrogen atom reacting with the oxygen ions bound to both Ni and YSZ to produce hydroxyl (Charge transfer reaction 1), the latter reacting with the other hydrogen atom to form water (Charge transfer reaction 2). The predictive capability of this reaction mechanism to represent our experimental results was evaluated. The simulated Tafel plots were compared with our experimental data for a wide range of  $H_2$  and  $H_2O$  partial pressures and at different temperatures. Good agreements between simulation and experimental results were obtained. Charge transfer reaction 1 was found to dominate the overall charge transfer reaction under cathodic polarization. Under anodic polarization, a change in the dominating charge transfer reaction from charge transfer reaction 1 to charge transfer reaction 2 was found when increasing the  $H_2O$  partial pressure.

© 2013 Elsevier B.V. All rights reserved.

## 1. Introduction

A solid oxide fuel cell (SOFC) is a device that converts chemical energy directly into electrical energy with high efficiency. SOFCs can operate on a variety of fuels and have significantly less environmental impact than the traditional combustion systems [1–3]. Knowledge of the actual electrochemical oxidation occurring at the anode is of great importance for further improvement of the anode

performance. However, even for the simplest fuel,  $H_2$ , the detailed electrochemical reactions are not yet fully understood [4–6].

The electrochemical reactions occur at the triple phase boundary (TPB), where gas phase, anode and electrolyte join [4,7]. For reaction kinetic studies, pattern anodes have the advantage of forming a well-defined 2-D structure, thus avoiding the complicated 3-D structure effects on the electrochemical reactions that take place in cermet anodes. Moreover, influence of gas transport in porous media is eliminated in pattern anodes, and the TPB length of pattern anodes can be calculated accurately [5,8]. Yttria-Stabilized Zirconia (YSZ) is currently the most popular electrolyte material for SOFC, and Ni/YSZ pattern anodes have been commonly used in the characterization of electrochemical reaction mechanisms.

\* Corresponding author. Tel.: +1 (519) 888 4567x36472, +1 (519) 888 4567x32295; fax: +1 (519) 746 4979.

E-mail address: [ecroiset@uwaterloo.ca](mailto:ecroiset@uwaterloo.ca) (E. Croiset).

In order to elucidate the hydrogen electrochemical reaction mechanism on the Ni/YSZ anodes, extensive experimental and modelling studies have been performed so far, and several reaction mechanisms for hydrogen electro-oxidation have been proposed.

Bieberle and Gauckler [9] assumed that the charge transfer reaction is oxygen spillover from YSZ surface to Ni surface. In their work, a kinetic model describing a six-step elementary reaction mechanism was developed and validated using experimental results from Bieberle et al. [8]. The rate-limiting process was claimed to be either adsorption/desorption of hydrogen or removal of oxygen ions from YSZ. In addition, both processes could be coupled with charge transfer reaction and contributed to the rate-determining steps. However, effects of water on the anode performance were evaluated in a small range of water concentration for both modelling and experimental studies ( $\text{H}_2\text{O}$ : 0.04–2% at 700 °C). Also, no studies were performed under cathodic conditions. Moreover, their experimental results varied considerably from samples to samples [4].

Vogler et al. [4] investigated different charge transfer reactions by comparing simulation results with the experimental data reported by Bieberle et al. [9]. Hydrogen spillover with water formation on YSZ surface was claimed to be the mechanism which correctly predicts the observed relationship between polarization resistance and  $\text{H}_2$  and  $\text{H}_2\text{O}$  partial pressures. They also claimed that hydrogen spillover to oxide ions, water dissociation on YSZ, water desorption from YSZ, and surface diffusion of hydroxyl ions adsorbed on YSZ might be possible dominating processes. Due to lack of experimental data, the simulation was performed within a limited range of conditions ( $\text{H}_2\text{O}$ : 0.04–2%).

Goodwin et al. [10] assumed that hydrogen spills over to the YSZ surface to form hydroxyl, which subsequently spills over back to Ni surface with water formation on Ni surface. They claimed that this mechanism provides a good fit to the experimentally observed Tafel plots reported by Mizusaki et al. [11]. However, both experiment and simulation were conducted in a small range of gas compositions ( $\text{H}_2$ : 1–10%,  $\text{H}_2\text{O}$ : 0.4–1.7%).

Based on density functional theory (DFT), Shishkin and Ziegler [12] proposed that the  $\text{H}_2$  oxidation occurs primarily on the oxygen ions at the interface between Ni and  $\text{ZrO}_2$  (or  $\text{Y}_2\text{O}_3$ ). DFT study revealed that oxygen vacancy formation at the interface of Ni/YSZ was more favourable than at the Ni or YSZ surface. The easier vacancy formation directly leads to more negative charges transferring from YSZ to Ni surface. Moreover, it was found that the energy barrier for water formation at the interface is lower than that on Ni or YSZ surface. These indicate that the pathway of charge transfer reactions occurring at the interface is more feasible than oxygen and hydrogen spillover pathways.

The main goal of this study is to perform a kinetic study based on the charge transfer reactions proposed by Shishkin and Ziegler (2010) and evaluate the capability of this model to represent experimentally observed behaviour of  $\text{H}_2$  oxidation on Ni/YSZ pattern anodes.

A kinetic model representing surface chemical reactions, electrochemical reactions, and surface diffusion of the  $\text{H}_2/\text{H}_2\text{O}$  system on a SOFC pattern anode was developed and built in gPROMS.

Similar to the experimental procedure, Tafel plots were simulated under a wide range of  $\text{H}_2$  partial pressure ( $p_{\text{H}_2}$ ) ( $1 \times 10^4 \text{ Pa}$ – $9 \times 10^4 \text{ Pa}$ ) and  $\text{H}_2\text{O}$  partial pressure ( $p_{\text{H}_2\text{O}}$ ) ( $3 \times 10^3 \text{ Pa}$ – $5 \times 10^4 \text{ Pa}$ ) conditions. The simulated Tafel plots upon variation of  $p_{\text{H}_2}$  were compared with the Tafel plots obtained through experiments at 700 °C. This temperature was chosen because previous modelling results were also reported at 700 °C, and most of the parameters are available in the literature at this temperature. In addition, simulated Tafel plots upon variation of  $p_{\text{H}_2\text{O}}$  were compared with experimental Tafel plots at 550 °C. As presented in our previous

studies [13], stable structure and precise TPB length could be obtained when the pattern anode was tested under high amount of  $\text{H}_2\text{O}$  (>10%) conditions at 550 °C, but not at 700 °C.

At 700 °C, thermodynamic and kinetic parameters for surface chemical reactions were taken from Vogler et al. [4]. Activation energies and changes in Gibbs free energy for charges transfer reactions were taken from Shishkin and Ziegler [12]. Pre-exponential factors for the charge transfer reactions were treated as free fit parameters. At 550 °C, more parameters were treated as free fit parameters (to be discussed later) due to lack of data in the literature at this temperature.

## 2. Methodology

### 2.1. Experimental

The electrolyte used in this study is an 8 mol%  $\text{Y}_2\text{O}_3$  stabilized  $\text{ZrO}_2$  single crystal disc with (100) orientation (MTI corporation), and the thickness of the electrolyte is 0.5 mm. Ni/YSZ pattern anodes with Ni thickness of 1  $\mu\text{m}$  were fabricated. A photolithographic process with bi-layer resist system was used for constructing Ni patterns on YSZ surface. Details of the fabrication process can be found in a previous study [13]. Platinum (Pt) cathode and the Pt reference electrode with thickness of 100 nm were prepared by DC magnetron sputtering. The Pt cathode (not patterned) was placed symmetrically to the pattern anode on the opposite side of the YSZ single crystal. A three electrodes configuration was applied to characterize the Ni/YSZ pattern anode electrochemical behaviour. The detailed description of the three electrodes and the electrochemical test set-up can also be found in our previous study [13]. The cell was first pre-treated in  $\text{H}_2/\text{H}_2\text{O}$  environments to achieve stable performance. Then, the Tafel plots were measured using a Solartron Electrochemical Interface 1287 in the potentiostatic mode under different  $p_{\text{H}_2}$  ( $3 \times 10^4 \text{ Pa} \leq p_{\text{H}_2} \leq 9 \times 10^4 \text{ Pa}$ ) and  $p_{\text{H}_2\text{O}}$  ( $3 \times 10^3 \text{ Pa} \leq p_{\text{H}_2\text{O}} \leq 5 \times 10^4 \text{ Pa}$ ) conditions. The imposed overpotential for Tafel plots measurements were between –0.4 and 0.4 V.

### 2.2. Modelling approach

In traditional fuel cells models, the electrochemistry is described by global reactions and the current density is calculated based on the Butler–Volmer equation. This simplified approach cannot fully represent the complex processes occurring at the triple phase boundary [14]. In this work, detailed 1-D models representing the coupled behaviour of surface chemistry, electrochemistry and surface diffusion were developed. Similar models were also used in previous studies [4,8,10]. The model describes not only the electrochemical reactions, but also the non-faradaic chemical reactions and surface-diffusive transport on Ni and YSZ surfaces. The reaction rates of these chemical and electrochemical reactions were obtained through mass-action kinetics. The current density was calculated directly via charge transfer reactions. Both steady-state and dynamic electrode behaviour can be simulated with these models.

A Ni/YSZ pattern anode half-cell configuration, which was used in both Goodwin et al. [10] and Vogler et al.'s [4] studies, was chosen for this study. To mimic the experimental conditions, the cell consists of a dense YSZ disk as the supporting electrolyte, an array of thin, straight Ni strips on one side of the electrolyte, a Pt counter electrode, and a Pt reference electrode on the other side. Due to the symmetry of the pattern anode, only one domain is considered for the simulation. This domain extends from the centre line of the Ni strip to the centre line of the adjacent YSZ strip. As shown in Fig. 1,  $d_{\text{Ni}}$ ,  $d_{\text{YSZ}}$  are the width of Ni and YSZ strips,

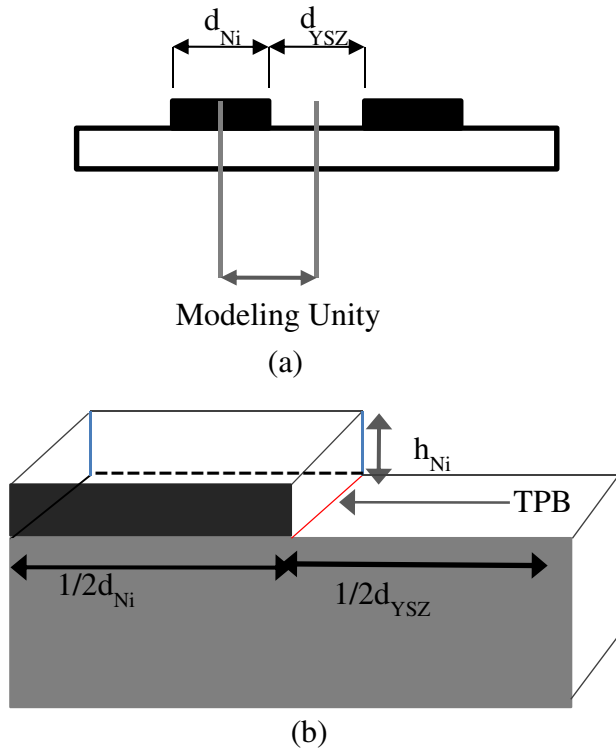


Fig. 1. (a) Side view of the pattern anode, (b) the half-cell model.

respectively, and  $h_{Ni}$  is the thickness of the Ni layer. The red line in Fig. 1(b) is the TPB line.

### 2.3. Governing equations

#### 2.3.1. Elementary chemical reactions

Both Ni and YSZ surface chemical reactions in this study are written as reversible elementary reaction steps. The general form of the chemical reaction is expressed as:



where  $m$  represents all the reactions that include adsorption/desorption of gas phase species, and surface reactions,  $A_i$ ,  $B_i$ ,  $C_i$  and  $D_i$  are species involved in these reactions,  $k_{f,m}$  and  $k_{r,m}$  are the forward and reverse reaction-rate constants, respectively, and the units are given in terms of mol, cm and s.

The reaction rate for forward and reverse reactions can be represented using Equations (2)–(9). The forward reaction rate constants are calculated using Arrhenius expression, and the reverse reaction rate constants are obtained based on a thermodynamically consistent way [15,16].

$$r_{f,m} = k_{f,m} \prod_{i \in R_{f,m}} c_i^{v_i'} \quad (2)$$

$$k_{f,m} = k_{f,m}^0 T^{\beta_m} \exp\left(-\frac{E_{f,m}^{\text{act}}}{RT}\right) \quad (3)$$

$$r_{r,m} = k_{r,m} \prod_{i \in R_{r,m}} c_i^{v_i''} \quad (4)$$

$$k_{r,m} = k_{f,m} \exp\left(\frac{\Delta G_m}{RT}\right) \quad (5)$$

$$\Delta G_m = \sum_{i \in R_{f,m}} v_{i,m}' (h_i - Ts_i) - \sum_{i \in R_{r,m}} v_{i,m}'' (h_i - Ts_i) \quad (6)$$

$$h_i = h_{0,i} + C_p (T - T_{\text{ref}}) \quad (7)$$

$$C_p = a' + \frac{b'}{2} (T + T_{\text{ref}}) \quad (8)$$

$$s_i = s_{0,i} + a' (\ln T - \ln T_{\text{ref}}) + b' (T - T_{\text{ref}}) \quad (9)$$

Here,  $r_{f,m}$  and  $r_{r,m}$  represent the forward and reverse reaction rates ( $\text{mol s}^{-1} \text{cm}^{-2}$ ),  $c_i$  is the area-specific concentration of species  $i$  ( $\text{mol cm}^{-2}$ ),  $v_i'$ ,  $v_i''$  are stoichiometric coefficients of species  $i$  in the forward and reverse reactions,  $k_{f,m}^0$  is the pre-exponential factor of the forward reaction,  $E_{f,m}^{\text{act}}$  is the activation energy for the forward reaction ( $\text{J mol}^{-1}$ ), and  $\beta_m$  is a temperature coefficient.  $\Delta G_m$  is the Gibbs free energy change of the reaction ( $\text{J mol}^{-1}$ );  $h_i$  ( $\text{J mol}^{-1}$ ) and  $s_i$  ( $\text{J K}^{-1} \text{mol}^{-1}$ ) are molar enthalpy and molar entropy of species  $i$  at temperature  $T$  (K).  $h_{0,i}$  and  $s_{0,i}$  are molar enthalpy and molar entropy of species  $i$  at reference state temperature ( $T_{\text{ref}}: 25^\circ\text{C}$ ),  $C_p$  is the average specific heat over the temperature range involved.  $a'$  and  $b'$  are constants used for average specific heat calculation.

The concentration change of surface species  $i$  due to chemical reactions is given as [15]:

$$\frac{dc_i}{dt} = \sum_i (v_i' r_{f,m} - v_i'' r_{r,m}) \quad (10)$$

For surface chemistry, the reaction rate is usually expressed in the form of surface coverage ( $\theta_i$ ), which is defined as [8]:

$$\theta_i = c_i / N_k \quad (11)$$

$$\sum \theta_i = 1$$

where  $N_k$  is the area-specific density of Ni or YSZ ( $\text{mol cm}^{-2}$ ). The surface coverage of each species  $i$  is between 0 and 1, and the total surface coverage of all the species is 1. The unfilled surface sites are also considered as one individual species [10].

#### 2.3.2. Charge transfer (CT) reactions

Charge transfer reaction rates directly determine the faradaic current produced. They are expressed in the same way as those for the chemical reactions [4,8,17].

$$r_{\text{CT},k} = k_{\text{CT},f} \prod_{i \in R_{f,k}} c_i^{v_i'} - k_{\text{CT},r} \prod_{i \in R_{r,k}} c_i^{v_i''} \quad (12)$$

$$k_{\text{CT},f} = k_{\text{CT},f}^0 \exp\left(-\frac{E_{\text{CT},f}}{RT}\right) \exp\left(\frac{\alpha n F \eta}{RT}\right) \quad (13)$$

$$k_{\text{CT},r} = k_{\text{CT},r}^0 \exp\left(-\frac{E_{\text{CT},r}}{RT}\right) \exp\left(\frac{\Delta G_{\text{CT}}}{RT}\right) \exp\left(-\frac{(1-\alpha)nF\eta}{RT}\right) \quad (14)$$

where  $r_{\text{CT},k}$  is the net reaction rate of the charge transfer reaction  $k$  ( $\text{mol s}^{-1} \text{cm}^{-2}$ ),  $k_{\text{CT},f}$ ,  $k_{\text{CT},r}$  are forward and reverse reaction rate constants ( $\text{cm}^3 \text{mol}^{-1} \text{s}^{-1}$ ),  $k_{\text{CT},f}^0$  ( $\text{cm}^3 \text{mol}^{-1} \text{s}^{-1}$ ) and  $E_{\text{CT},f}$  ( $\text{J mol}^{-1}$ )

**Table 1**

Elementary reaction steps and kinetic parameters used in the work, which are taken from Vogler et al. (2009).

	Reversible reactions	Pre-exponential factor ( $k_m^0$ )	Activation energy ( $E_m^{\text{act}}$ ) (kJ mol <sup>-1</sup> )	$\beta_m$
1	$\text{H}_2\text{O}_{\text{gas}} + (\text{YSZ}) \xrightleftharpoons[k_{-1}]{k_1} \text{H}_2\text{O}_{\text{YSZ}}$	$6.6 \times 10^{11} \text{ cm}^3 \text{ mol}^{-1} \text{ s}^{-1}$	0	0.5
2	$\text{O}_{\text{YSZ}}^{2-} + \text{H}_2\text{O}_{\text{YSZ}} \xrightleftharpoons[k_{-2}]{k_2} 2\text{OH}_{\text{YSZ}}^-$	$1.6 \times 10^{22} \text{ cm}^2 \text{ mol}^{-1} \text{ s}^{-1}$	9.6	0
3	$\text{V}_\text{O}(\text{YSZ}) + \text{O}_{\text{YSZ}}^{2-} \xrightleftharpoons[k_{-3}]{k_3} \text{O}_\text{O}^{\text{X}}(\text{YSZ}) + (\text{YSZ})$	$1.6 \times 10^{22} \text{ cm}^2 \text{ mol}^{-1} \text{ s}^{-1}$	90.9	0
4	$\text{H}_2\text{O}_{\text{gas}} + (\text{Ni}) \xrightleftharpoons[k_{-4}]{k_4} \text{H}_2\text{O}_{\text{Ni}}$	$1.4 \times 10^{10} \text{ cm}^3 \text{ mol}^{-1} \text{ s}^{-1}$	0	0.5
5	$\text{H}_2 \text{ gas} + 2(\text{Ni}) \xrightleftharpoons[k_{-5}]{k_5} 2\text{H}_{\text{Ni}}$	$9.8 \times 10^{17} \text{ cm}^5 \text{ mol}^{-1} \text{ s}^{-1}$	0	0.5
6	$\text{H}_{\text{Ni}} + \text{O}_{\text{Ni}} \xrightleftharpoons[k_{-6}]{k_6} \text{OH}_{\text{Ni}} + (\text{Ni})$	$5.0 \times 10^{22} \text{ cm}^2 \text{ mol}^{-1} \text{ s}^{-1}$	97.0	0
7	$\text{H}_2\text{O}_{\text{Ni}} + \text{O}_{\text{Ni}} \xrightleftharpoons[k_{-7}]{k_7} 2\text{OH}_{\text{Ni}}$	$5.4 \times 10^{23} \text{ cm}^2 \text{ mol s}$	20.9	0
8	$\text{OH}_{\text{Ni}} + \text{H}_{\text{Ni}} \xrightleftharpoons[k_{-8}]{k_8} \text{H}_2\text{O}_{\text{Ni}} + (\text{Ni})$	$3.0 \times 10^{20} \text{ cm}^2 \text{ mol}^{-1} \text{ s}^{-1}$	43.0	0

are pre-exponential coefficient and activation energy of the forward reaction respectively,  $\Delta G_{\text{CT}}$  (J mol<sup>-1</sup>) is the Gibbs free energy change of the charge transfer reaction,  $n$  is the number of electrons transferred in the electrochemical reaction,  $\alpha$  is the transfer coefficient,  $\eta$  is the overpotential, and  $F$  is the Faraday constant (96,487 C mol<sup>-1</sup>).

The faradaic current density produced due to a charge transfer reaction is described as [18]:

$$j_F = nFL_{\text{TPB}}r_{\text{CT},k}, \quad j_{F,T} = \sum_{\text{all CTRs}} j_F \quad (15)$$

where  $j_F$  is the current density (A cm<sup>-2</sup>),  $L_{\text{TPB}}$  is the TPB length (cm cm<sup>-2</sup>). The total current density  $j_{F,T}$  is the sum of current density produced by all the charge transfer reactions.

### 2.3.3. Surface diffusion

Surface species diffusion is given by Fick's law, as shown in Equation (16) [4,15].

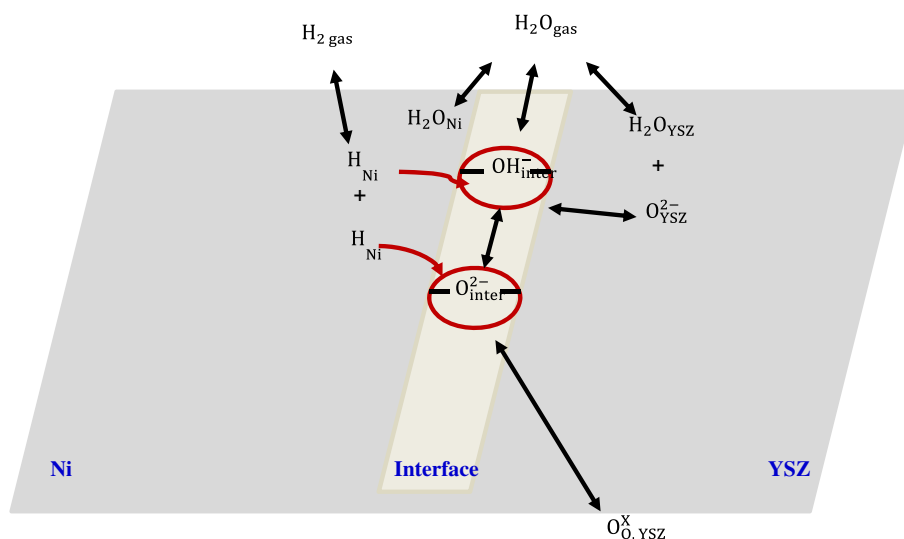
**Table 2**

Surface diffusion parameters taken from Vogler et al. (2009).

Species	$D_i^0$ (cm <sup>2</sup> s <sup>-1</sup> )	$E_i^{\text{act}}$ (kJ mol <sup>-1</sup> )
H <sub>Ni</sub>	$4.6 \times 10^{-3}$	14.4
O <sub>Ni</sub>	$6.3 \times 10^{-3}$	61.3
OH <sub>Ni</sub>	$6 \times 10^{-3}$	30.5
H <sub>2</sub> O <sub>Ni</sub>	$6 \times 10^{-3}$	28.0
O <sub>YSZ</sub> <sup>2-</sup>	$5.5 \times 10^{-7}$	90.0
H <sub>2</sub> O <sub>YSZ</sub>	$1.3 \times 10^{-2}$	55.0
OH <sub>YSZ</sub>	$1.3 \times 10^{-2}$	55.0

$$J_i = -D_i \frac{dc_i}{dz} \quad (16)$$

$$D_i = D_i^0 \exp\left(-\frac{E_i^{\text{act}}}{RT}\right) \quad (17)$$

**Fig. 2.** Schematic illustration of hydrogen oxidation at the interface of Ni/YSZ.

**Table 3**

Thermodynamic parameters for surface species at 700 °C and 25 °C.

Species	$h_i$ at 25 °C (kJ mol <sup>-1</sup> )	$s_i$ at 25 °C (J mol <sup>-1</sup> K <sup>-1</sup> )	$h_i$ at 700 °C (kJ mol <sup>-1</sup> )	$s_i$ at 700 °C (J mol <sup>-1</sup> K <sup>-1</sup> )
H <sub>2</sub> O <sub>gas</sub>	-241.8	188.8	-217.0 <sup>b</sup>	232.0 <sup>b</sup>
H <sub>2</sub> gas	0	130.7	20.0 <sup>b</sup>	165.0 <sup>b</sup>
H <sub>2</sub> O <sub>YSZ</sub>	-291.9	49.3	-273.0	98.0
O <sub>YSZ</sub> <sup>2-</sup>	-183.5	0 <sup>a</sup>	-236.0	0
OH <sub>YSZ</sub>	-270.3 <sup>a</sup>	62.5 <sup>a</sup>	-283.0	67.0
YSZ	0	0	0	0
H <sub>2</sub> O <sub>Ni</sub>	-302.6	87.6	-273.0	130.0
H <sub>Ni</sub>	-48.3 <sup>a</sup>	28.3	-32.0	41.0
O <sub>Ni</sub>	-237.5	19.4	-222.0	39.0
OH <sub>Ni</sub>	-214.6	75.8	-193.0	106.0
Ni	0	0	0	0
V <sub>O</sub>	0	0	0	0
O <sub>O</sub> <sup>x</sup>	-192.0 <sup>a</sup>	0	-236.0	0

The other parameters at 25 °C and 700 °C are taken from Habibzadeh [19] and Vogler et al. [4], respectively.

<sup>a</sup> Free fit parameters.

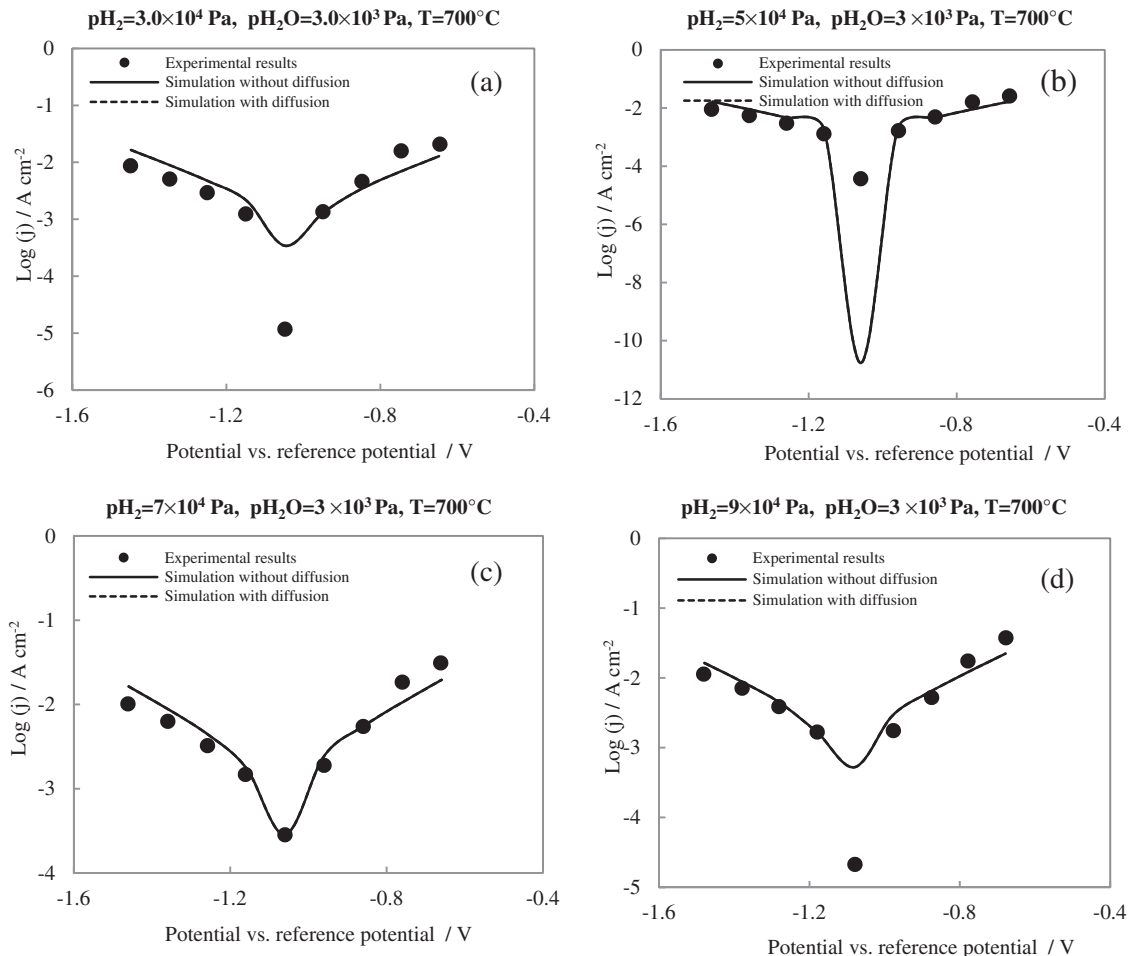
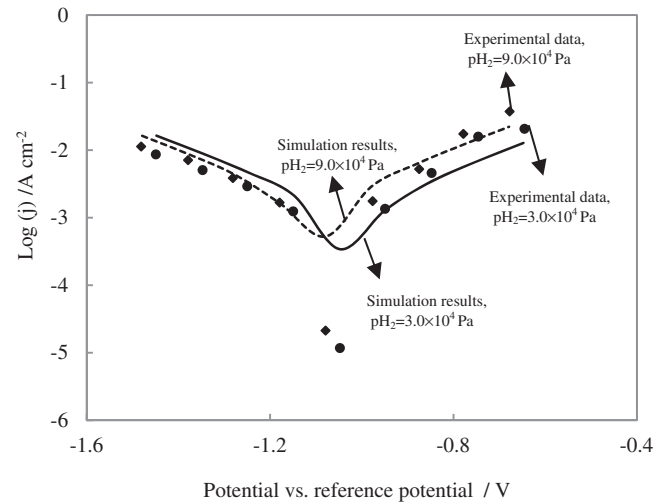
<sup>b</sup> Taken from O'Hayre et al. [2].

**Table 4**

Kinetic and thermodynamic parameters used for charge transfer reactions.

	700 °C	550 °C
$k_s^0$ (cm <sup>3</sup> mol <sup>-1</sup> s <sup>-1</sup> )	$3.5 \times 10^{10}$	$3.5 \times 10^{10}$
$k_{10}^0$ (cm <sup>3</sup> mol <sup>-1</sup> s <sup>-1</sup> )	$2.0 \times 10^{25}$	$2.0 \times 10^{25}$
$\Delta G_{CT1}$ (kJ mol <sup>-1</sup> )	6.31	4.30
$\Delta G_{CT2}$ (kJ mol <sup>-1</sup> )	-88.8	-68.7
$\Delta E_{CT1}$ (kJ mol <sup>-1</sup> )	13.0 <sup>a</sup>	45.0
$\Delta E_{CT2}$ (kJ mol <sup>-1</sup> )	154.9 <sup>a</sup>	154.9 <sup>a</sup>

<sup>a</sup> Taken from Shishkin and Ziegler (2010), the others are all fitted parameters.

**Fig. 3.** Comparison between experimental and simulation Tafel plots upon variation of pH<sub>2</sub> at 700 °C.pH<sub>2</sub>O=3.0×10<sup>3</sup> Pa, T=700 °C**Fig. 4.** Effect of pH<sub>2</sub> on the current density at 700 °C.

where  $J_i$  is the surface flux of adsorbate  $i$  (mol cm<sup>-2</sup> s<sup>-1</sup>),  $c_i$  is the concentration of species  $i$  (mol cm<sup>-3</sup>),  $D_i$  is the surface diffusion coefficient of species  $i$  (cm<sup>2</sup> s<sup>-1</sup>),  $z$  is the distance along the surface perpendicular to the TPB line (cm),  $D_i^0$  is the pre-exponential constant (cm<sup>2</sup> s<sup>-1</sup>), and  $E_i^{\text{act}}$  is the activation energy (J mol<sup>-1</sup>).

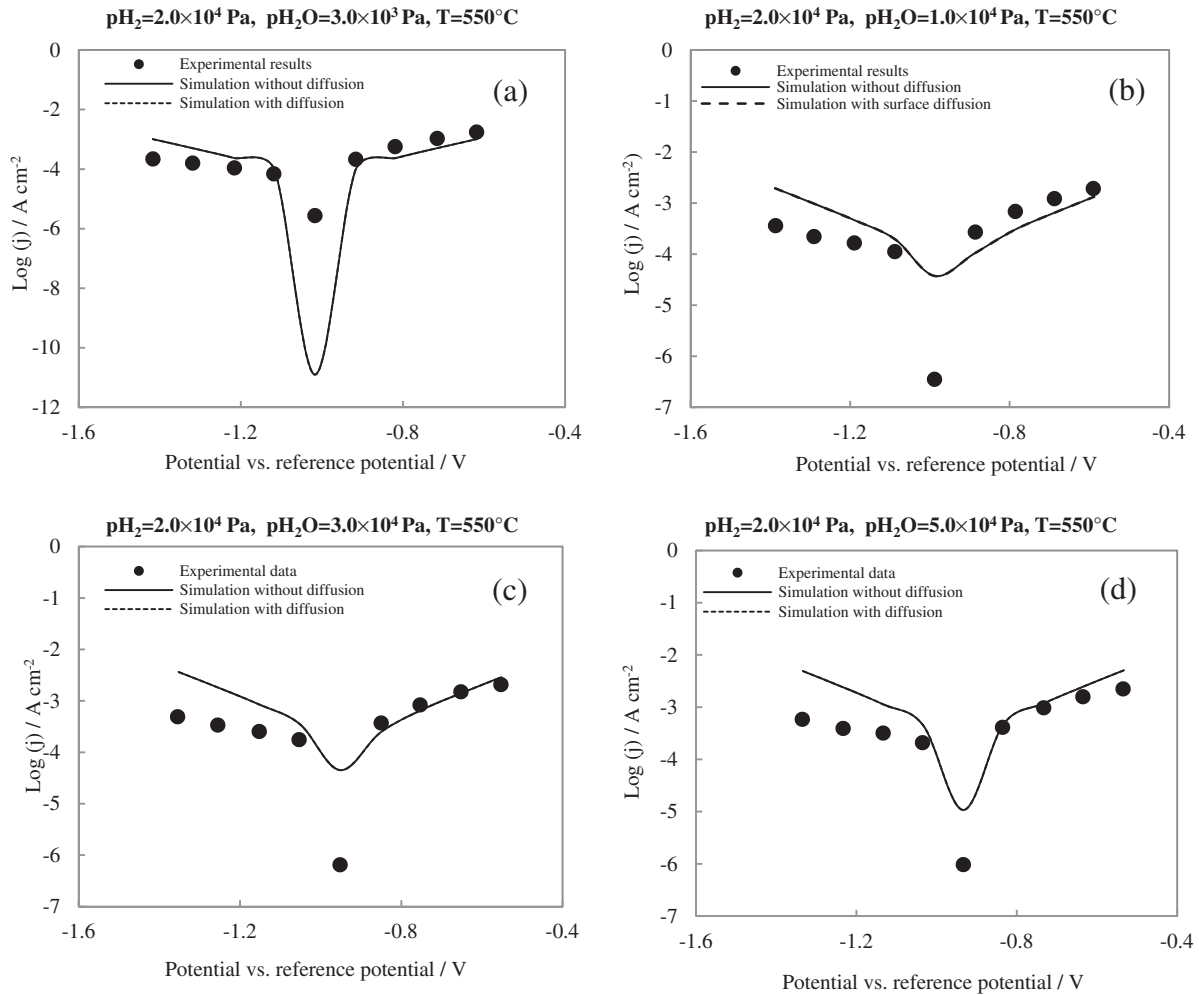


Fig. 5. Comparison between experimental and simulated Tafel plots upon variation of  $\text{pH}_2\text{O}$  at 550 °C.

The surface concentration change for each adsorbed species  $i$ , which is described in Equation (18), is determined by both chemical reaction and surface diffusion [4].

$$\frac{dc_i}{dt} = \sum_i (v_i' r_{f,m} - v_i'' r_{r,m}) - \frac{dj_i}{dz} \quad (18)$$

Because of the symmetry of the model, the boundary conditions are [10]:

At  $z = -0.5d_{\text{Ni}}$  and  $z = 0.5d_{\text{YSZ}}$ ,

$$J_i = 0 \quad (19)$$

At the TPB line, for reactant species directly involved in the charge transfer reactions,

$$J_i = -j_F/nF \quad (20)$$

For product species directly involved in the charge transfer reactions,

$$J_i = j_F/nF \quad (21)$$

For those surface species that are not involved in charge transfer reactions,

$$J_i = 0 \quad (22)$$

#### 2.4. Investigation of hydrogen oxidation at Ni/YSZ interface

In this study, chemical reactions on the Ni surface were referred from Bieberle and Gauckler (2002), Vogler et al. (2009) and Goodwin et al. (2009). The YSZ surface reactions were the same as

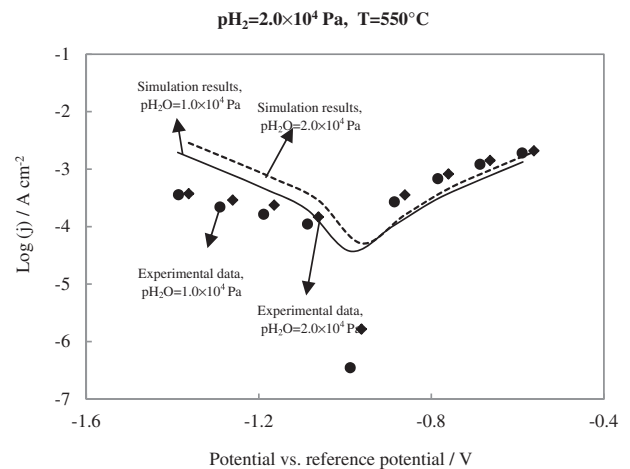


Fig. 6. Effect of  $\text{pH}_2\text{O}$  on the current density at 550 °C.



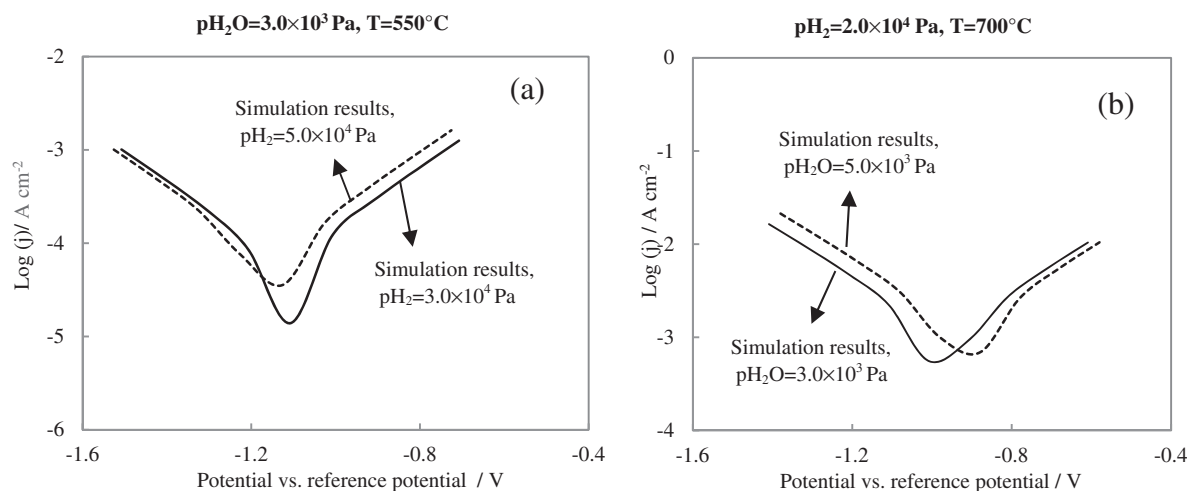
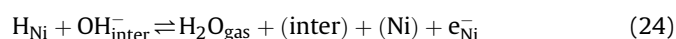
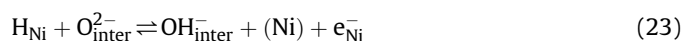


Fig. 7. Effect of  $p\text{H}_2$  and  $p\text{H}_2\text{O}$  on the current density at 550 °C and 700 °C, respectively.

used in Vogler et al. [4]. Charge transfer reactions are based on DFT study performed by Shishkin and Ziegler [12]. Table 1 summarizes the elementary reaction steps on Ni and YSZ surfaces, as well as the corresponding kinetic parameters (pre-exponential factors and activation energy for forward reactions at 700 °C used in this work).

Regarding the charge transfer reactions, Shishkin and Ziegler [12] claimed that oxygen vacancy formation at the interface of Ni/YSZ is more favourable than at the YSZ surface, which results in more negative charges being transferred from YSZ to Ni surface. Moreover, it was found that the energy barrier of water formation at the interface was lower than that on Ni or YSZ surface. These indicate that charge transfer reactions occurring at the interface are more likely than oxygen and hydrogen spillover. In addition, water produced at the interface is assumed to be in the gas phase, since the energy barrier for water desorption from the interface is very small, based on DFT calculation [12]. The charge transfer reactions are listed in reactions (23) and (24), and schematically demonstrated in Fig. 2.  $\text{H}_2$  oxidation at the Ni/YSZ interface involves a hydrogen atom reacting with the oxygen ions bound to both Ni and YSZ surfaces to produce hydroxyl ion, which reacts with the other hydrogen atom to form water.



In this reaction mechanism, there are two gas phase species ( $\text{H}_2$ ,  $\text{H}_2\text{O}$ ), four Ni surface species ( $\text{H}_{\text{Ni}}$ ,  $\text{O}_{\text{Ni}}$ ,  $\text{OH}_{\text{Ni}}$ ,  $\text{H}_2\text{O}_{\text{Ni}}$ ), three YSZ surface species ( $\text{H}_2\text{O}_{\text{YSZ}}$ ,  $\text{O}_{\text{YSZ}}^{2-}$ ,  $\text{OH}_{\text{YSZ}}^-$ ), two bulk species (lattice oxygen ( $\text{O}_{\text{O}}^{\text{x}}$ ) and oxygen vacancy ( $\text{V}_{\text{O}}^{\text{x}}$ )), and three species at the interface ( $\text{O}_{\text{inter}}^{2-}$ ,  $\text{OH}_{\text{inter}}^-$ , and free surface (inter)). The Ni free surface (Ni) and YSZ free surface (YSZ) are also considered as two single species. At 700 °C, Shishkin and Ziegler [12] calculated the activation energy for the forward reactions of the charge transfer reactions, and found 13  $\text{kJ mol}^{-1}$  and 154.9  $\text{kJ mol}^{-1}$  for charge reactions (23) and (24), respectively. Changes in Gibbs free energy of the charge transfer reactions obtained through DFT calculation are 113  $\text{kJ mol}^{-1}$  and -75.4  $\text{kJ mol}^{-1}$ , respectively. Surface diffusion parameters are taken from Vogler et al. [4] and are listed in Table 2.

### 3. Results and discussion

Thermodynamic parameters for surface species at 25 °C and 700 °C used in the model are shown in Table 3. Kinetic and

thermodynamic parameters for charge transfer reactions were either taken from Shishkin and Ziegler or determined through fitting the experimental results. Those parameters are given in Table 4.

At 700 °C, the activation energy of charge transfer reactions (Reactions (23) and (24)) were taken from Shishkin and Ziegler [12]. It was realized that the location for the minimum of the logarithm of the current density on the Tafel plots depends on the Gibbs free energy change of both charge transfer reactions. This Gibbs free energy changes were then adjusted for best fit, resulting in a value of 6.31  $\text{kJ mol}^{-1}$  for Reaction (23) and a value of -88.8  $\text{kJ mol}^{-1}$  for Reaction (24). It is also important to notice that one would expect a current density close to zero at OCV, but the experimental and simulation results give a baseline current. For the experimental data, the reason for a baseline current is due to the chemical potential difference between the cathode and anode, which leads to a small exchange current density at equilibrium conditions. Gas leaks, as well as electronic leaks, may also cause a small exchange current density. For the simulation, the value of the minimum current density is extremely sensitive to very small changes in the value of the Gibbs free energy. For example, in Fig. 3(b), the set of Gibbs free energies yields a very small current density ( $\log(i) = -10.76 \text{ A cm}^{-2}$ ). Would we change the value of those free energies by less than 0.5%, the logarithm of the minimum current density would increase to -6.0  $\text{A cm}^{-2}$ . Note that changes in Gibbs free energy of this magnitude, although they did affect significantly the minimum value of the current density, they did not have any effect on the values of the cathodic and anodic current densities. Also, note that the value of 6.31  $\text{kJ mol}^{-1}$  for Reaction (23) is significantly smaller than the calculated value through DFT (113  $\text{kJ mol}^{-1}$ ) by Shishkin and Ziegler. The Gibbs free energy change of the overall  $\text{H}_2$  oxidation reaction is the sum of the Gibbs free energy change of all the elementary reactions. With the fitting value (6.31  $\text{kJ mol}^{-1}$ ), the sum of the Gibbs free energy change of all the elementary reactions is much closer to the Gibbs free energy change of the overall  $\text{H}_2$  reaction than when using the DFT calculated value.

At 550 °C, charges in Gibbs free energy as well as the activation energy for Reaction (23) were treated as a free fit parameter to obtain good fitting between simulation and experimental results. The activation energy for Reaction (24) had insignificant effect on the simulation results, and was taken from the DFT calculation.

In Fig. 3, both simulation and experimental results regarding the effect of  $\text{H}_2$  partial pressure on current density

**Table 5**  
Surface coverages of Ni and YSZ surface species changes with  $p_{H_2}$  and  $p_{H_2O}$  when the overpotential is 0.3 V.

	$\theta(H_{2O_{Ni}})$	$\theta(H_{Ni})$	$\theta(O_{Ni})$	$\theta(OH_{Ni})$	$\theta(Ni)$	$\theta(H_2O_{YSZ})$	$\theta(O_{YSZ}^-)$	$\theta(OH_{YSZ}^-)$	$\theta(YSZ)$	$\theta(O_{inter}^{2-})$	$\theta(OH_{inter}^-)$	$\theta(inter)$
$p_{H_2}$ (Pa) constant $p_{H_2O}$ : $3.0 \times 10^3$ Pa 700 °C	$1.0 \times 10^4$	$1.76 \times 10^{-9}$	$1.35 \times 10^{-3}$	$1.61 \times 10^{-3}$	$2.66 \times 10^{-8}$	$7.48 \times 10^{-12}$	0.800	$1.12 \times 10^{-3}$	0.199	0.800	$1.12 \times 10^{-3}$	0.199
	$2.0 \times 10^4$	$1.76 \times 10^{-9}$	$1.92 \times 10^{-3}$	$8.07 \times 10^{-4}$	$1.88 \times 10^{-8}$	$7.48 \times 10^{-12}$	0.800	$1.12 \times 10^{-3}$	0.199	0.800	$1.12 \times 10^{-3}$	0.199
	$3.0 \times 10^4$	$1.76 \times 10^{-9}$	$2.35 \times 10^{-3}$	$5.38 \times 10^{-4}$	$1.53 \times 10^{-8}$	$7.48 \times 10^{-12}$	0.800	$1.12 \times 10^{-3}$	0.199	0.800	$1.12 \times 10^{-3}$	0.199
	$5.0 \times 10^4$	$1.76 \times 10^{-9}$	$3.03 \times 10^{-3}$	$3.23 \times 10^{-4}$	$1.19 \times 10^{-8}$	$7.48 \times 10^{-12}$	0.800	$1.12 \times 10^{-3}$	0.199	0.800	$1.12 \times 10^{-3}$	0.199
	$7.0 \times 10^4$	$1.76 \times 10^{-9}$	$3.58 \times 10^{-3}$	$2.30 \times 10^{-4}$	$1.00 \times 10^{-8}$	$7.48 \times 10^{-12}$	0.800	$1.12 \times 10^{-3}$	0.199	0.800	$1.12 \times 10^{-3}$	0.199
$p_{H_2O}$ (Pa) constant $p_{H_2}$ : $2.0 \times 10^4$ Pa 550 °C	$9.0 \times 10^4$	$1.76 \times 10^{-9}$	$4.06 \times 10^{-3}$	$1.79 \times 10^{-4}$	$8.84 \times 10^{-9}$	$7.48 \times 10^{-12}$	0.800	$1.12 \times 10^{-3}$	0.199	0.800	$1.12 \times 10^{-3}$	0.199
	$3.0 \times 10^3$	$3.99 \times 10^{-9}$	$4.49 \times 10^{-3}$	$4.46 \times 10^{-5}$	$2.40 \times 10^{-9}$	$9.09 \times 10^{-11}$	0.800	$1.93 \times 10^{-3}$	0.199	0.800	$1.93 \times 10^{-3}$	0.199
	$1.0 \times 10^3$	$1.33 \times 10^{-8}$	$4.49 \times 10^{-3}$	$1.49 \times 10^{-4}$	$7.99 \times 10^{-9}$	$3.02 \times 10^{-10}$	0.798	$3.50 \times 10^{-3}$	0.198	0.798	$3.50 \times 10^{-3}$	0.198
	$3.0 \times 10^4$	$3.99 \times 10^{-8}$	$4.49 \times 10^{-3}$	$4.46 \times 10^{-4}$	$2.40 \times 10^{-8}$	$9.05 \times 10^{-10}$	0.796	$6.05 \times 10^{-3}$	0.198	0.796	$6.05 \times 10^{-3}$	0.198
	$5.0 \times 10^4$	$6.64 \times 10^{-8}$	$4.49 \times 10^{-3}$	$7.43 \times 10^{-4}$	$4.00 \times 10^{-8}$	$1.51 \times 10^{-9}$	0.795	$7.80 \times 10^{-3}$	0.197	0.795	$7.80 \times 10^{-3}$	0.197

are presented. The simulation and experimental conditions are:  $3 \times 10^4$  Pa  $\leq p_{H_2} \leq 9 \times 10^4$  Pa,  $p_{H_2O} = 3 \times 10^3$  Pa,  $T = 700$  °C.

In Fig. 3 (as well as in Fig. 5) the simulation results from models with and without surface diffusion overlap exactly, which means that the surface diffusion is fast under the above operating conditions. On both Ni and YSZ surfaces, surface coverage profiles are uniform. The experimental results can be well reproduced by simulation under each  $p_{H_2}$  condition. Fig. 4 shows that  $p_{H_2}$  has positive effects on the current density under anodic polarization, and the effect of  $p_{H_2}$  on the cathodic current density is less pronounced, which agrees well with the experimental data. As seen in Fig. 4, the experimentally observed anodic current density increases when increasing  $p_{H_2}$ , and the experimental cathodic current density is almost independent of  $p_{H_2}$ .

Fig. 5 evaluates the influence of  $p_{H_2O}$  on the current density for both experiments and simulation. The simulation and experimental conditions are:  $3 \times 10^3$  Pa  $\leq p_{H_2O} \leq 5 \times 10^4$  Pa,  $p_{H_2} = 2 \times 10^4$  Pa,  $T = 550$  °C. The effect of surface diffusion on both anodic and cathodic current density is negligible. Under high cathodic potential, the simulated current density is larger than the experimental current density, but simulation results still reasonably predict the experimental data. As shown in Fig. 6, the experimentally observed decrease in cathodic current density with increasing  $p_{H_2O}$  can be reproduced by the simulation. For both modelling and experimental results, the effect of  $p_{H_2O}$  on anodic current density is small.

In order to compare the simulation results with the experimental results, the effect of  $p_{H_2}$  on current densities was simulated at 700 °C and the effect of  $p_{H_2O}$  on current densities was simulated at 550 °C, which are presented in Fig. 7. As mentioned earlier, it was not possible to conduct a complete kinetic study experimentally at 700 °C because the Ni/YSZ pattern anodes experienced significant structure changes at this temperature for  $H_2O$  greater than 10%. Nonetheless, effect of  $H_2O$  at 700 °C can be studied from simulation. Fig. 7 shows the dependence of simulated current density on  $p_{H_2O}$  at 700 °C as well as the effect of  $p_{H_2}$  on current density at 550 °C. The effect of  $p_{H_2}$  on current density at 550 °C could have been done experimentally, but it was deemed sufficient here to conduct this study of  $p_{H_2}$  effect on current density only with simulated results. At both 550 °C and 700 °C, surface diffusion does not show any effects on the current density under different  $p_{H_2}$  and  $p_{H_2O}$  conditions. At 550 °C,  $p_{H_2}$  has a positive effect on the anodic current density and a very weak effect on cathodic current density, which is similar to the simulation results obtained at 700 °C. At 700 °C, the cathodic current density increases when increasing  $p_{H_2O}$ , whereas the dependence of anodic current density on  $p_{H_2O}$  is much weaker. This is also consistent with the simulation results obtained at 550 °C.

Table 5 presents the surface coverage of Ni and YSZ surface species for various  $p_{H_2}$  and  $p_{H_2O}$  conditions when an overpotential of 0.3 V is imposed. When increasing both  $p_{H_2}$  and  $p_{H_2O}$ , Ni free sites slightly decrease. With an increase in  $p_{H_2}$ ,  $\theta(H_{Ni})$  increases, but  $\theta(O_{Ni})$  and  $\theta(OH_{Ni})$  decrease. Surface coverage of  $H_2O_{Ni}$  and YSZ surface species are slightly affected by  $p_{H_2}$ .  $\theta(O_{YSZ}^-)$  slightly decreases, and  $\theta(OH_{YSZ}^-)$  increases. When increasing  $p_{H_2O}$ , surface coverage of  $O_{YSZ}^{2-}$  decreases and more  $H_2O_{YSZ}$  and  $OH_{YSZ}^-$  are generated. In addition, the amount of  $H_2O_{Ni}$ ,  $O_{Ni}$  and  $OH_{Ni}$  increase, and  $H_{Ni}$  almost remains constant with increasing  $p_{H_2O}$ . At the Ni/YSZ interface, surface coverage of  $OH_{inter}^-$  slightly increases and  $\theta(O_{inter}^{2-})$  shows small decrease with increasing both  $p_{H_2}$  and  $p_{H_2O}$ .

As discussed before, the anodic current density increases with an increase in  $p_{H_2}$ . Therefore, the trend of current density change is related to the change in  $\theta(H_{Ni})$  and  $\theta(OH_{inter}^-)$  upon variation of  $p_{H_2}$  under constant  $p_{H_2O}$  and constant temperature. When increasing



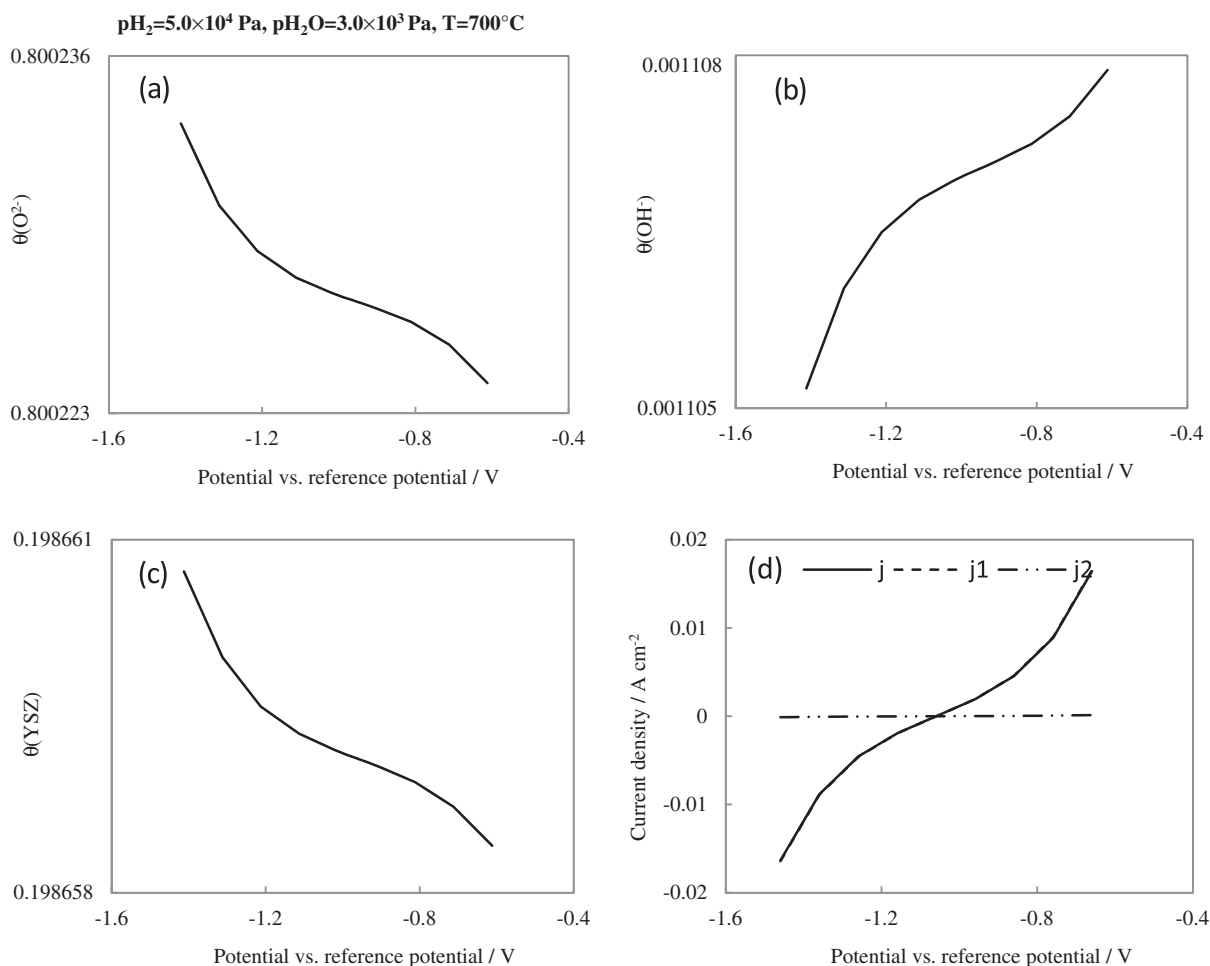


**Fig. 8.** Dependence of surface coverages of YSZ surface species and current densities on electrode potential:  $p\text{H}_2 = 5.0 \times 10^4 \text{ Pa}$ ,  $p\text{H}_2\text{O} = 3.0 \times 10^3 \text{ Pa}$ ,  $T = 700^\circ\text{C}$ .

$p\text{H}_2$ ,  $\theta(\text{H}_{\text{Ni}})$  and  $\theta(\text{OH}_{\text{inter}}^-)$  increases and leads to an increase in anodic current density. Under cathodic polarization, the extent of  $\theta(\text{H}_{\text{Ni}})$  change is the same as that under anodic polarization when increasing the same amount of  $\text{H}_2$ . But, the extent of  $\theta(\text{OH}_{\text{inter}}^-)$  change under cathodic polarization is smaller than under anodic polarization. This explains the strong dependence of the anodic current density and the weak dependence of the cathodic current density on  $p\text{H}_2$ . When  $p\text{H}_2$  and temperature are kept constant, the current density increases when increasing  $p\text{H}_2\text{O}$ , and the trend of current density changes is mainly related to  $\theta(\text{OH}_{\text{inter}}^-)$  changes. According to the charge transfer reactions (23) and (24), electrons produced are directly related to  $\theta(\text{H}_{\text{Ni}})$ ,  $\theta(\text{OH}_{\text{inter}}^-)$  and  $\theta(\text{O}_{\text{inter}}^{2-})$ . Under constant  $p\text{H}_2$  and constant temperature,  $\theta(\text{H}_{\text{Ni}})$  is almost constant, and  $\theta(\text{O}_{\text{inter}}^{2-})$  decreases with an increase in  $p\text{H}_2\text{O}$  leading to more  $\theta(\text{OH}_{\text{inter}}^-)$  production, which explains the increase in current density. In addition, the extent of  $\theta(\text{OH}_{\text{inter}}^-)$  change is bigger under cathodic polarization than under anodic polarization when increasing the same amount of  $\text{H}_2\text{O}$ . This is the reason why the cathodic current density depends more strongly on  $p\text{H}_2\text{O}$  than the anodic current density does.

Under constant  $p\text{H}_2$  and  $p\text{H}_2\text{O}$  conditions,  $\theta(\text{H}_2\text{O}_{\text{Ni}})$  and  $\theta(\text{H}_{\text{Ni}})$  increase with decreasing temperature, while surface coverages of other Ni surface species decrease. On the YSZ surface,  $\theta(\text{H}_2\text{O}_{\text{YSZ}})$  and  $\theta(\text{OH}_{\text{YSZ}}^-)$  increases when decreasing the temperature. Surface coverages of other YSZ surface species remain constant with a decrease in temperature. At the interface,  $\theta(\text{OH}_{\text{inter}}^-)$  increases when decreasing temperature.

On Ni surface, surface coverage of different species are not influenced by varying the electrode potential. But surface coverage of species on YSZ surface slightly change when changing the electrode potential. As shown in Fig. 8(a)–(c), from cathodic polarization to anodic polarization, surface coverage of  $\text{OH}_{\text{YSZ}}^-$  increases by about 1.78%, and the surface coverage of other YSZ surface species slightly decrease.  $\theta(\text{O}_{\text{YSZ}}^{2-})$  decreases by about 0.0013%, and surface coverage of free YSZ surface decreases by about 0.005%. Although the changes of  $\theta(\text{O}_{\text{YSZ}}^{2-})$  and  $\theta(\text{YSZ})$  are very small and almost negligible, a noticeable difference in current density is caused. Fig. 8(d) describes the effect of electrode potential on total current density ( $j$ ) as well as current density contributed by charge transfer reaction (23) ( $j_1$ ) and (24) ( $j_2$ ). The total current density is the sum of  $j_1$  and  $j_2$ . Fig. 8(d) shows that the total current density is mainly due to  $j_1$  under the operating conditions for this figure. The contribution of current density from reaction (24) is small. Therefore, the charge transfer reaction (23) dominates the overall charge transfer reaction for  $\text{H}_2$  oxidation.

Under anodic polarization, the trend of  $\theta(\text{OH}_{\text{YSZ}}^-)$  change with electrode potential is consistent with the trend of current density changes when  $p\text{H}_2$  and  $p\text{H}_2\text{O}$  are kept constant. The overall  $\text{H}_2$  oxidation becomes faster with an increase in  $\theta(\text{OH}_{\text{YSZ}}^-)$ .

Under cathodic polarization, current density change with electrode potential follow the trend of changes in  $\theta(\text{O}_{\text{YSZ}}^{2-})$  and free YSZ surface. With more free YSZ surface, the overall  $\text{H}_2$  oxidation accelerates and the generated current density increases. Similar behaviour was observed when changing  $p\text{H}_2$ , while keeping  $p\text{H}_2\text{O}$  ( $3.0 \times 10^3 \text{ Pa}$ ) and temperature ( $700^\circ\text{C}$ ) constant.

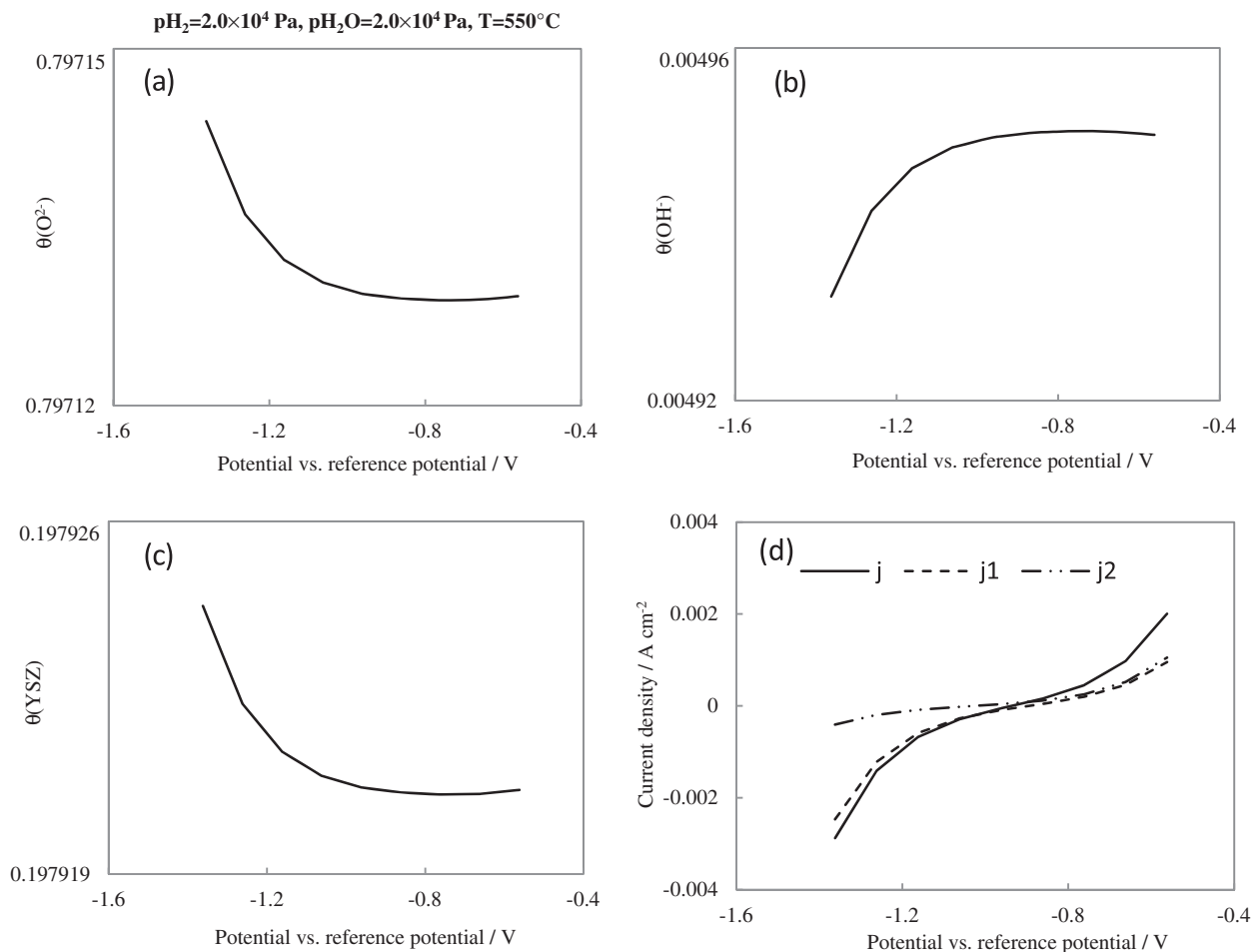


Fig. 9. Dependence of surface coverages of YSZ surface species and current densities on electrode potential:  $p_{H_2} = 2.0 \times 10^4$  Pa,  $p_{H_2O} = 2.0 \times 10^4$  Pa,  $T = 550$  °C.

Fig. 9 shows the changes at 550 °C in various surface species and current density when varying the electrode potential. At 550 °C, the effect of electrode potential on surface coverages of YSZ surface species and current density was evaluated under different  $p_{H_2O}$  conditions. When  $p_{H_2O}$  is  $3.0 \times 10^3$  Pa, the dependence of surface coverages and current density on electrode potential is very similar to what was observed at 700 °C under the same  $p_{H_2O}$  condition (not shown here). With further increase in  $p_{H_2O}$  to  $2.0 \times 10^4$  Pa, surface coverage of  $OH_{YSZ}^{2-}$  increases and surface coverages of  $O_{YSZ}^{2-}$ ,  $H_2O_{YSZ}$  and free YSZ surface decrease with a decrease in cathodic potential. Surface coverages of all the species remain constant under anodic polarization (see Fig. 9(a)–(c)). In Fig. 9(d), the total cathodic current density is mainly due to  $j_1$ , and  $j_2$  has minor effect on the total cathodic current density. Under anodic polarization,  $j_1$  is similar to  $j_2$  and the current density from both charge transfer reactions equally affects the total current density. Therefore, charge transfer reaction (23) dominates the whole charge transfer reaction under cathodic polarization, and both charge transfer reactions ((23) and (24)) are rate controlling under anodic polarization.

In Fig. 10, changes in surface coverage as well as current density upon variation of electrode potential are presented when the partial pressure of  $H_2O$  is  $5.0 \times 10^4$  Pa. Under cathodic conditions, surface coverage of  $OH_{YSZ}^{2-}$  increases and surface coverages of  $O_{YSZ}^{2-}$ ,  $H_2O_{YSZ}$  and free YSZ surface decrease with decreasing cathodic potential, which is similar to surface coverage changes under other  $p_{H_2O}$  conditions. The current density from charge transfer reaction (23) is still the main contributor to the total current density. Under anodic polarization, surface coverage of  $OH_{YSZ}^{2-}$  decreases and

surface coverages of  $O_{YSZ}^{2-}$ ,  $H_2O_{YSZ}$  and free YSZ surface increase when decreasing anodic potential, which is opposite to surface coverage changes when  $p_{H_2O}$  is  $3.0 \times 10^3$  Pa. The total anodic current density is mainly from charge transfer reaction (24), and charge transfer reaction (23) has minor influence on the total anodic current density. Charge transfer reaction (24) dominates the overall charge transfer reaction.

Under cathodic polarization, the charge transfer reaction (23) proceeds towards generating H and  $O^{2-}$  species, which leads to an increase in  $\theta(O^{2-})$  and a decrease in  $\theta(OH^-)$  when increasing the cathodic potential.

Under anodic polarization, the charge transfer reaction (23) proceeds towards the production of hydroxyl ions and electrons, which results in an increase in  $\theta(OH^-)$  and a decrease in  $\theta(O^{2-})$  when decreasing the anodic potential at low value of  $p_{H_2O}$  is low ( $3.0 \times 10^3$  Pa). When increasing  $p_{H_2O}$ , more hydroxyl ions are produced through reaction 2, as seen in Table 1, which increases the reaction rate of charge transfer reaction (24). The increase of  $OH^-$  also leads to more  $O^{2-}$  production through reaction (23), which explains the increase of  $\theta(O^{2-})$  under anodic polarization when  $p_{H_2O}$  is high ( $5.0 \times 10^4$  Pa).

At 700 °C, simulated results similar to what was observed at 550 °C were obtained when varying  $p_{H_2O}$ .

The good agreement between the simulation and experimental data in a wide range of  $p_{H_2}$  and  $p_{H_2O}$  conditions reveals that the new charge transfer reactions mechanism proposed by Shishkin and Ziegler [12] can reasonably predict the experimentally observed behaviour of Ni/YSZ pattern anode in  $H_2/H_2O$

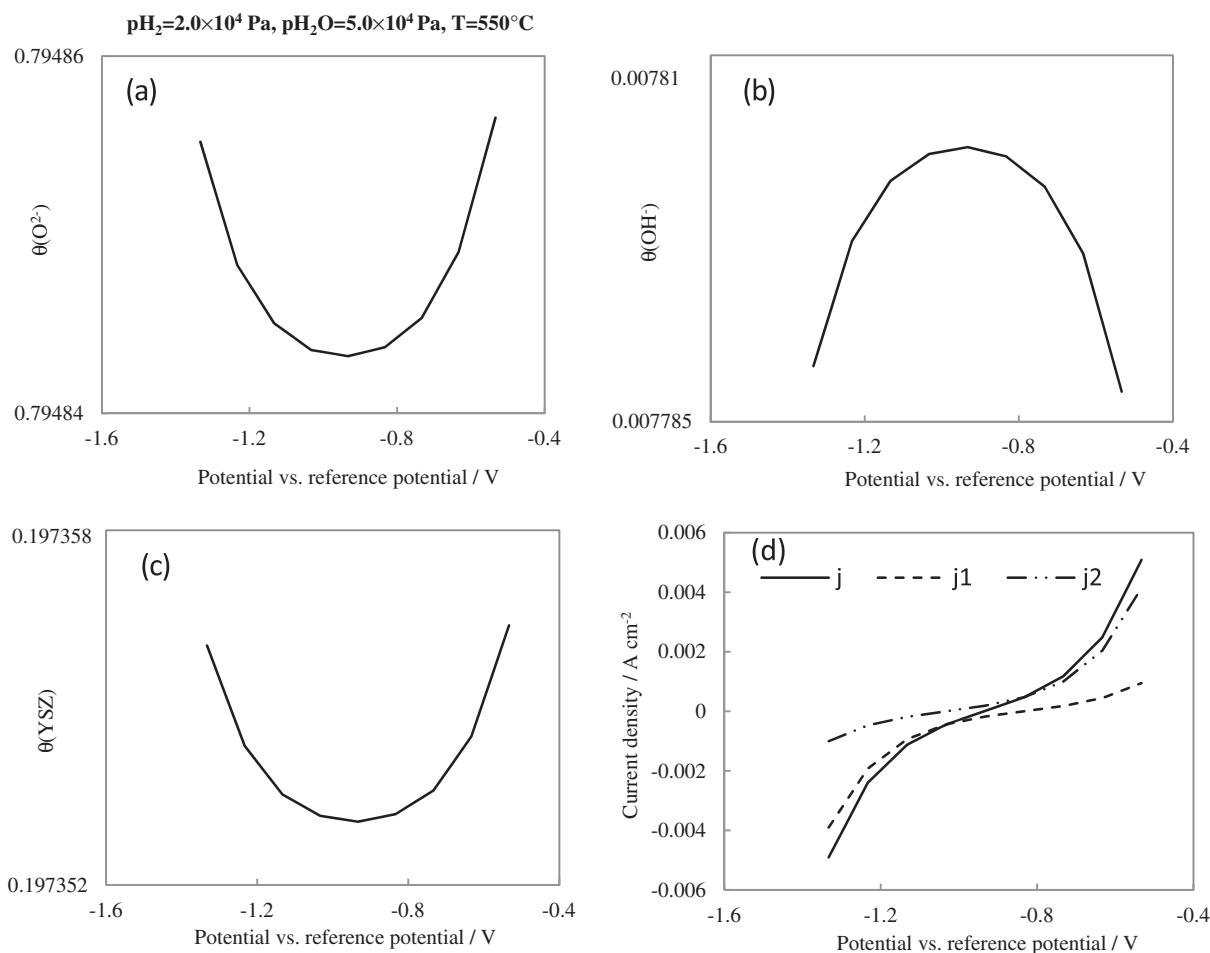
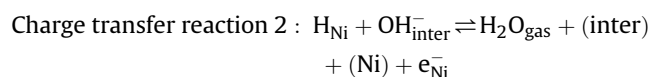


Fig. 10. Dependence of surface coverages of YSZ surface species and current densities on electrode potential:  $p_{\text{H}_2} = 2.0 \times 10^4$  Pa,  $p_{\text{H}_2\text{O}} = 5.0 \times 10^4$  Pa,  $T = 550$  °C.

environments. Surface diffusion is fast and does not affect the pattern anode performance. Under cathodic polarization, the dominating charge transfer reaction (reaction (23)) does not change when varying the temperature and partial pressures of  $\text{H}_2$  and  $\text{H}_2\text{O}$ . Under anodic polarization, the dominating charge transfer reaction (still reaction (23)) does not change when changing  $p_{\text{H}_2}$  and temperature. However, it changes from charge transfer reaction (23) to charge transfer reaction (24) when increasing the partial pressure of  $\text{H}_2\text{O}$  from  $3.0 \times 10^3$  Pa to  $5.0 \times 10^4$  Pa.

#### 4. Conclusions

This work presents a kinetic modelling study of  $\text{H}_2$  electrochemical oxidation using Ni/YSZ pattern anodes as model anodes. The model represents elementary reactions of  $\text{H}_2$  oxidation on Ni/YSZ pattern anodes. Surface reactions, electrochemical reactions and surface diffusions are described in the model. The charge transfer reactions mechanism proposed by Shishkin and Ziegler [12] was implemented into the kinetic model and applied to interpret our experimental results. The two charge transfer reactions are:



The main results are summarized as follows.

- Experimental data (both anodic and cathodic currents in the Tafel plots) can be well reproduced by simulation under a wide range of  $p_{\text{H}_2}$  and  $p_{\text{H}_2\text{O}}$  conditions.
- It was found that the effect of surface diffusion on the pattern anode performance is negligible under all conditions in this work.
- Under cathodic polarization, charge transfer reaction 1 is always the dominating charge transfer reaction, irrespective of  $p_{\text{H}_2}$ ,  $p_{\text{H}_2\text{O}}$  and temperature.
- Under anodic polarization, the dominating charge transfer reaction switches from charge transfer reaction 1 to charge transfer reaction 2 when increasing the partial pressure of  $\text{H}_2\text{O}$  from  $3.0 \times 10^3$  Pa to  $5.0 \times 10^4$  Pa.

#### Acknowledgements

This research was supported through funding to the NSERC Solid Oxide Fuel Cell Canada Strategic Research Network from Natural Science and Engineering Research Council (NSERC) and other sponsors listed at [www.sofccanada.ca](http://www.sofccanada.ca). The authors gratefully acknowledge Dr. Maxim Shishkin and Dr. Tom Ziegler at the University of Calgary for helpful discussions about this work.

#### Nomenclature

Roman symbols

$A_i, B_i, C_i, D_i$  species involved chemical reactions

$a', b'$  constants

$c_i$	area-specific concentration of surface species $i$ (mol cm <sup>-2</sup> )
$D_i$	diffusion coefficient of surface species $i$ (cm <sup>2</sup> s <sup>-1</sup> )
$D_i^0$	pre-exponential constants (cm <sup>2</sup> s <sup>-1</sup> )
$d_{\text{elyt}}$	electrolyte thickness (cm)
$E_{\text{CT},f}$	activation energy for forward charge transfer reaction (kJ mol <sup>-1</sup> )
$E_i^{\text{act}}$	activation energy for surface diffusion (kJ mol <sup>-1</sup> )
$F$	Faraday constant (96487 C mol <sup>-1</sup> )
$\Delta G$	Gibbs free energy change of the reaction (kJ mol <sup>-1</sup> )
$h_i$	molar enthalpy (kJ mol <sup>-1</sup> )
$h_{0,i}$	molar enthalpy at reference state temperature (kJ mol <sup>-1</sup> )
$j$	current density (A cm <sup>-2</sup> )
$j_F$	Faradic current density (A cm <sup>-2</sup> )
$j_{F,T}$	total faradic current density (A cm <sup>-2</sup> )
$J_i$	molar flux of surface species $i$ (mol cm <sup>-1</sup> s <sup>-1</sup> )
$k_{f,m}$	forward reaction rate constant (mol, cm, s)
$k_{r,m}$	reverse reaction rate constant (mol, cm, s)
$k_{f,m}^0$	pre-exponential coefficient for the forward reaction (mol, cm, s)
$n$	electron number transferred during an electrochemical reaction
$N_k$	area-specific density (mol cm <sup>-2</sup> )
$p$	pressure (Pa)
$r$	reaction rate (mol cm <sup>-2</sup> s <sup>-1</sup> )
$R$	gas constant (8.314 J K <sup>-1</sup> mol <sup>-1</sup> )
$R_p$	polarization resistance ( $\Omega$ cm <sup>2</sup> )
$s_i$	molar entropy (J mol <sup>-1</sup> K <sup>-1</sup> )
$s_0$	molar entropy at reference state temperature (J mol <sup>-1</sup> K <sup>-1</sup> )
$T$	temperature (K)
$v_i$	stoichiometric factor of species $i$ in forward reaction
$v_i$	stoichiometric factor of species $i$ in reverse reaction
$z$	distance along the surface perpendicular to the TPB line (cm)

#### Greek symbols

$\alpha$	transfer coefficient
$\eta$	overpotential (V)
$\theta$	surface coverage

#### Subscripts

act	activation
-----	------------

CT	charge transfer reaction
CTRs	charge transfer reactions
elyt	electrolyte
F	Faraday
f,m	forward reaction
H <sub>2</sub>	hydrogen
$i$	surface species
$k$	Ni or YSZ surface
m	adsorption, desorption and surface reactions
r,m	reverse reaction

#### Abbreviation

DFT	density functional theory
Ni	nickel
SOFC	solid oxide fuel cell
TPB	triple phase boundary
YSZ	yttria-stabilised-zirconia

#### References

- [1] N.Q. Minh, T. Takahashi, *Science and Technology of Ceramic Fuel Cells*, first ed., Elsevier Science, 1995, p. 378.
- [2] R. O'Hayre, S. Cha, W. Colella, F.B. Prinz, *Fuel Cell Fundamentals*, John Wiley & Sons, Hoboken, NJ, 2006, p. 409.
- [3] B. Boer de, PhD Thesis, University of Twente, Twente, 1998.
- [4] M. Vogler, A. Bieberle-Hütter, L. Gauckler, J. Warnatz, W.G. Bessler, *J. Electrochem. Soc.* 156 (2009) B663–B672.
- [5] A. Utz, H. Störmer, A. Leonide, A. Weber, E. Ivers-Tiffée, *J. Electrochem. Soc.* 157 (2010) B920.
- [6] V. Yurkiv, A. Utz, A. Weber, E. Ivers-Tiffée, H.R. Volpp, W.G. Bessler, *Electrochim. Acta* (2011).
- [7] J. Mizusaki, H. Tagawa, T. Saito, *J. Electrochem. Soc.* 141 (1994) 2129–2134.
- [8] A. Bieberle, L.P. Meier, L.J. Gauckler, *J. Electrochem. Soc.* 148 (2001) A646–A656.
- [9] A. Bieberle, L.J. Gauckler, *Solid State Ionics* 146 (2002) 23–41.
- [10] D.G. Goodwin, H. Zhu, A.M. Colclasure, R.J. Kee, *J. Electrochem. Soc.* 156 (2009) B1004–B1021.
- [11] J. Mizusaki, H. Tagawa, T. Saito, T. Yamamura, K. Kamitani, K. Hirano, S. Ehara, T. Takagi, T. Hikita, M. Ippommatsu, S. Nakagawa, K. Hashimoto, *Solid State Ionics* 70–71 (1994) 52–58.
- [12] M. Shishkin, T. Ziegler, *J. Phys. Chem. C* 114 (2010) 11209–11214.
- [13] W. Yao, E. Croiset, *J. Power Sources* 226 (2013) 162–172.
- [14] W.G. Bessler, S. Gewies, M. Vogler, *Electrochim. Acta* 53 (2007) 1782–1800.
- [15] H.S. Fogler (Ed.), *Elements of Chemical Reaction Engineering*, third ed., Prentice Hall PTR, Upper Saddle River, N.J., 1999.
- [16] X. Li, *Principles of Fuel Cells*, first ed., Taylor & Francis, 2005, p. 592.
- [17] Y. Shi, C. Li, N. Cai, *J. Power Sources* 196 (2011) 5526–5537.
- [18] W.G. Bessler, *Solid State Ionics* 176 (2005) 997–1011.
- [19] B. Habibzadeh, *Understanding CO Oxidation in SOFC'S Using Nickel Patterned Anode*, University of Maryland, USA, 2007 (PhD Thesis).